

Enabling ultra-flexible inorganic thin-film-based thermoelectric devices by introducing nanoscale titanium layers

Received: 26 May 2024

Accepted: 7 January 2025

Published online: 14 January 2025

 Check for updates

Ming Tan  ^{1,2,6}, Xiao-Lei Shi  ^{2,6}, Wei-Di Liu ², Yong Jiang  ³, Si-Qi Liu  ², Tianyi Cao  ², Wenyi Chen ², Meng Li ², Tong Lin ¹, Yuan Deng  ⁴, Shaomin Liu  ⁵ & Zhi-Gang Chen  ² 

Here, we design exotic interfaces within a flexible thermoelectric device, incorporating a polyimide substrate, Ti contact layer, Cu electrode, Ti barrier layer, and thermoelectric thin film. The device features 162 pairs of thin-film legs with high room-temperature performance, using p-Bi_{0.5}Sb_{1.5}Te₃ and n-Bi₂Te_{2.7}Se_{0.3}, with figure-of-merit values of 1.39 and 1.44, respectively. The 10 nm Ti contact layer creates a strong bond between the substrate and the Cu electrode, while the 10 nm Ti barrier layer significantly reduces internal resistance and enhances the tightness between thermoelectric thin films and Cu electrodes. This enables both exceptional flexibility and an impressive power density of 108 $\mu\text{W cm}^{-2}$ under a temperature difference of just 5 K, with a normalized power density exceeding 4 $\mu\text{W cm}^{-2} \text{K}^{-2}$. When attached to a 50 °C irregular heat source, three series-connected devices generate 1.85 V, powering a light-emitting diode without the need for an additional heat sink or booster.

Thermoelectric materials and devices offer direct conversion between thermal energy (temperature differences, ΔT) and electrical energy, holding promise in fields such as waste heat recovery and solid-state cooling, aiming to alleviate pressure on fossil fuel consumption and environmental pollution¹. Currently, most commercialized thermoelectric devices are based on solid-state configurations, comprising pairs of p-type and n-type inorganic single or polycrystalline bismuth-telluride-based bulks connected electrically in series and thermally in parallel, sandwiched between rigid alumina substrates, with metal electrodes (such as copper) linking them¹. While these devices demonstrate high thermoelectric conversion efficiency, they struggle to effectively harness waste heat from irregular heat sources like human skin and drainage exhaust pipes². Special device designs (e.g., ring-shaped) can accommodate curved heat sources, but they require specific surface curvature, limiting their adaptability to various and

variably curved heat sources¹. While it is possible to attach a flexible secondary substrate to the hot side of solid-state devices to capture waste heat from irregular heat sources, the secondary substrate introduces a significant loss of ΔT , resulting in lower utilization efficiency and diminished output performance. Thus, developing thermoelectric materials and devices with certain flexibility is crucial and has become a recent research focus³.

Generally, higher thermoelectric performance of materials leads to greater energy conversion efficiency of the device. The thermoelectric potential of a material can be evaluated by $ZT = S^2\sigma T/\kappa$, where T denotes the absolute temperature, $S^2\sigma$ represents the power factor, composed of the Seebeck coefficient (S) and electrical conductivity (σ), reflecting the overall electrical transport capacity, and κ denotes the thermal conductivity, comprising electronic thermal conductivity (κ_e) and lattice thermal conductivity (κ_l)¹. κ_l is usually determined by

¹School of Textile Science and Engineering, Tiangong University, Tianjin, China. ²School of Chemistry and Physics, ARC Research Hub in Zero-emission Power Generation for Carbon Neutrality, and Centre for Materials Science, Queensland University of Technology, Brisbane, QLD, Australia. ³School of Electronics and Information Engineering, Tiangong University, Tianjin, China. ⁴Key Laboratory of Intelligent Sensing Materials and Chip Integration Technology of Zhejiang Province, Hangzhou Innovation Institute of Beihang University, Hangzhou, China. ⁵School of Engineering, Great Bay University, Dongguan, China.

⁶These authors contributed equally: Ming Tan, Xiao-Lei Shi.  e-mail: zhigang.chen@qut.edu.au

the micro/nanostructure of the material, and more complex structures with more multi-dimensional lattice defects usually lead to lower κ_l , but also lower σ due to carrier scattering at these crystal imperfections¹. Generally, to enable certain flexibility to thermoelectric devices, organic and organic/inorganic hybrid thermoelectric materials have been explored⁴. While organic materials exhibit ultra-high flexibility and low κ (owing to their macromolecular characteristics)⁵, their low S results in reduced $S^2\sigma$ and ZT , limiting device performance⁵. Similarly, carbon-based materials such as single-walled carbon nanotubes (SWCNTs) are flexible but suffer from excessive κ and low S ⁶. In contrast, inorganic thermoelectric materials and their devices demonstrate significantly higher thermoelectric performance and stability compared to carbon, organic, and organic/inorganic hybrid materials, leading to the rapid development of flexible devices based on inorganic materials in recent years⁷. To impart flexibility to these devices, besides reducing the size of bulk thermoelectric materials in the device (e.g., miniatures)⁸, approaches include using flexible substrates⁷ and special device designs (e.g., hinge-type)⁹, enabling these devices to maintain high output power (P) while retaining some flexibility. However, the interface issues between rigid materials and flexible substrates and electrodes continue to limit the flexibility of these devices⁷. Therefore, to further enhance the flexibility of flexible thermoelectric devices based on inorganic materials while maintaining their high thermoelectric performance, flexible inorganic thin-film materials have started to receive significant attention.

Currently, thin-film-based inorganic thermoelectric materials include bismuth/antimony tellurides (e.g., $\text{Bi}_2\text{Te}_{3-x}\text{Se}_x$ and $\text{Bi}_x\text{Sb}_{2-x}\text{Te}_3$)^{10,11}, silver chalcogenides (e.g., Ag_2S ¹², Ag_2Se ¹³, and Ag_2Te ¹⁴), other chalcogenides (e.g., SnSe ¹⁵, Cu_2Se ¹⁶, and TiS_2 ¹⁷), and oxide (e.g., ZnO)¹⁸, among others. So far, thermoelectric materials based on bismuth/antimony tellurides remain one of the best choices for near-room-temperature thermoelectric applications, owing to their narrow bandgap of approximately 0.1 eV, high inherent S , high σ , and low κ ^{10,11}. n-type materials, such as $\text{Bi}_2\text{Te}_{3-x}\text{Se}_x$, typically exhibit thermoelectric performance with $ZT > 1$ in the temperature range of 300–400 K^{10,11}, while p-type materials, such as $\text{Bi}_x\text{Sb}_{2-x}\text{Te}_3$, can achieve ZT values exceeding 1.2 in the same temperature range^{10,11}. Considering that most flexible thermoelectric devices use flexible substrates such as polyimide (PI) and other organic polymers⁷, which are not tolerant to high temperatures (e.g., over 300 °C which is the glass transition temperature of PI), these thin-film thermoelectric materials can be well-matched with these flexible organic polymer-based substrates in terms of operating temperature. At this point, to maximize the thermoelectric performance and flexibility of flexible devices based on bismuth/antimony telluride thin films, reasonable material design and optimization are required, while the materials themselves need to possess a certain level of flexibility⁷. This has become a focal point of research in recent years⁷. To enhance the flexibility of these materials, aside from nanostructuring their thickness⁷, reinforcement of their orientation structure can also improve flexibility¹⁹. However, despite the improvement in flexibility of the materials and the devices composed of them, interface issues remain unresolved⁷, resulting in the P of these flexible devices still being unable to match that of commercial solid-state devices. Moreover, whether thin-film materials can maintain the same high thermoelectric performance as bulk materials also poses a challenge to their preparation processes and design strategies⁷.

Till now, the structural design of flexible thermoelectric devices based on inorganic flexible films, particularly interface design, remains at a very preliminary stage^{7,20}. Many reported flexible devices based on thin-film thermoelectric materials simply used Ag paste to connect the thermoelectric legs on the PI substrates^{21–24}, with little consideration for contact issues between the films, electrodes, and substrates, resulting in impractical device designs and poor sustainability⁷. Some devices utilize inorganic metal materials as functional diffusion barrier

layers between thermoelectric materials and electrodes^{25,26}. However, there are few reports in flexible device design on enhancing the adhesion between electrodes and flexible substrates to improve overall device flexibility and stability^{27–31}. Additionally, previous flexible devices often applied ΔT s of tens or even hundreds of Kelvins to demonstrate their high power density (ω). However, in practical environments such as wearable thermoelectric devices on human skin, ΔT s are typically only a few Kelvin⁷. Moreover, due to the difficulty of mounting a heat sink at the cold side of flexible devices for power generation, the actual ΔT within the flexible devices is often only a few Kelvin⁷. In such small ΔT s, to enable truly practical applications of flexible thermoelectric devices, their ω or normalized power density (ω_T) must be sufficiently high to power low-grade electronics without the need for a heat sink or amplifier.

Results

Here, we present a highly flexible thermoelectric device with outstanding thermoelectric performance while maintaining high flexibility and stability. By combining magnetron sputtering and flip chip bonding techniques (Fig. 1a) and drawing inspiration from the classic structural design of commercial devices, we achieved flexible thermoelectric devices with outstanding performance. Especially, flip chip bonding is a high-density packaging connection technique²⁵. Compared to traditional flexible device packaging techniques, this technique offers several significant advantages, including high-density connections, easier conduction and dissipation of heat through the substrate, lower electrical resistance, as well as smaller and lighter dimensions²⁵. Our flexible device consists of 162 pairs of highly flexible thin films of p-type $\text{Bi}_{0.5}\text{Sb}_{1.5}\text{Te}_3$ (BST) and n-type $\text{Bi}_2\text{Te}_{2.7}\text{Se}_{0.3}$ (BTS) with high room-temperature ZT values (1.39 and 1.44, respectively). High-resolution photos of the as-fabricated devices can be found in Supplementary Figs. 1–2, and detailed fabrication procedures are provided in the experimental section. Through optimization of the magnetron sputtering process, the film orientation can be precisely controlled, combined with composition optimization to achieve carrier concentrations (hole carrier concentration n_p for p-type films and electron carrier concentration n_e for n-type films) close to the theoretical values for peak ZT (Fig. 1b, theoretical values obtained from single parabolic band (SPB) model calculations), we achieved near-perfect structural and compositional optimizations of the films. Due to the ultra-high thermoelectric performance of the films, our device exhibited an ultra-high ω of up to $108 \mu\text{W cm}^{-2}$ under a small ΔT of 5 K, as well as an ultra-high ω_T exceeding $4 \mu\text{W cm}^{-2} \text{K}^{-2}$, far surpassing previous reports (Fig. 1c)^{32–39}. Apart from the high thermoelectric performance of the thin films, the exceptional performance of our device also stems from the unique interface design of the PI substrate/Ti contact layer/Cu electrode/Ti barrier layer/thermoelectric thin film. The nano-sized Ti contact layer tightly bonds with the organic PI substrate and Cu electrode, resulting in exceptionally high device flexibility. It withstands over 100 bending cycles at a small bending radius r of 10 mm, with a resistance change rate ($\Delta R/R_0$) of only 3.3%. Additionally, the Ti barrier layer significantly reduces the internal resistance R_{in} of the device and enhances the tightness between the Cu electrode and the thermoelectric thin film, enabling the device to achieve both ultra-high P and flexibility. Three series-connected devices, attached to an irregular heat source at 50 °C (such as a heater pipe), can output a voltage of 1.85 V and illuminate a light-emitting diode (LED) without the need for any heat sink or booster (see the insets in Fig. 1c and high-resolution photo shown in Supplementary Fig. 3), demonstrating performance and high flexibility.

Thermoelectric performance and characterizations of thin films

As mentioned earlier, the high performance of our flexible thermoelectric device stems from the high thermoelectric properties of the flexible thin-film-based legs, with specific room-temperature

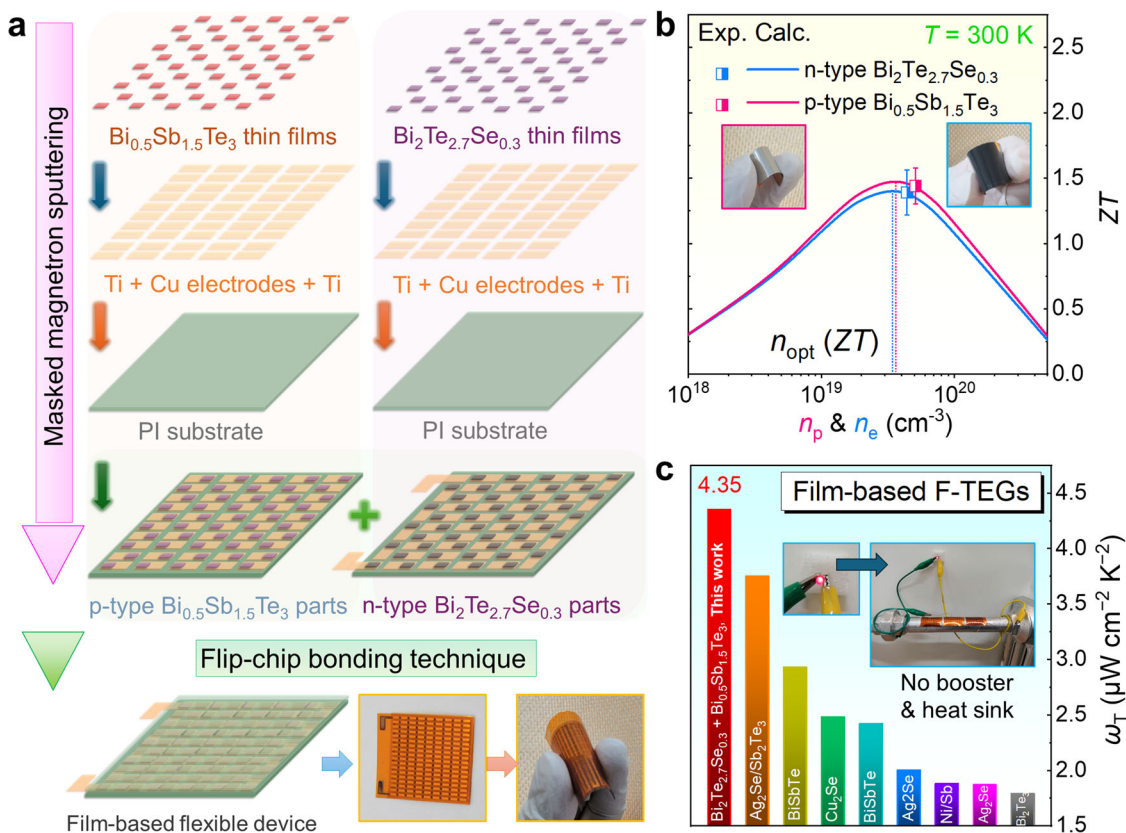


Fig. 1 | Introduction of high-performance and ultra-flexible thin-film-based thermoelectric devices. **a** Illustration of the fabrication process of the thermoelectric device. Here PI is abbreviated from polyimide. The photos of the as-fabricated devices in both flat and bent states are included as insets. **b** Comparison of experimental and calculated room-temperature ZT values of p-type and n-type thin films as thermoelectric legs in the flexible device. Here T is the absolute temperature, n_p is the hole carrier concentration for p-type thin films, n_e is the electron carrier concentration for n-type thin films, and n_{opt} is the carrier concentration that

can achieve peak ZT s. The photos of both p-type and n-type thin films in bent states are included as insets. Error bars represent the standard deviations of the ZT values. **c** Comparison of normalized output power density ω_T of the flexible thermoelectric generators (F-TEGs) between this work and reported works^{32–39}. The insets show that three flexible devices composed of 162 pairs of n/p flexible thin films can utilize the heat from a heating pipe to power light emitting diode (LED) bulbs, without requiring any booster or heat sink, at a pipe temperature of approximately 50 °C. The device assembly generates a voltage of around 1.85 V.

Table 1 | Room-temperature thermoelectric performance of thin films deposited on polyimide (PI) substrates

Composition	Type	σ (S cm^{-1})	S ($\mu\text{V K}^{-1}$)	$S^2\sigma$ ($\mu\text{W cm}^{-1} \text{K}^{-2}$)	n (10^{19}cm^{-3})	μ ($\text{cm}^2 \text{V}^{-1} \text{s}^{-1}$)	m'	E_{def} (eV)	κ ($\text{W m}^{-1} \text{K}^{-1}$)	κ_l ($\text{W m}^{-1} \text{K}^{-1}$)	ZT
$\text{Bi}_{0.5}\text{Sb}_{1.5}\text{Te}_3$	p	670	238	38.0	4.4	95.0	2.53 m_e	2.20	0.82	0.5	1.39
$\text{Bi}_2\text{Te}_{2.7}\text{Se}_{0.3}$	n	750	233	40.7	5.1	91.8	2.67 m_0	2.08	0.85	0.5	1.44

Here σ , S , $S^2\sigma$, n , μ , m' , E_{def} , κ , and κ_l denote electrical conductivity, Seebeck coefficient, power factor, carrier concentration, carrier mobility, effective mass, deformation potential, thermal conductivity, and lattice thermal conductivity, respectively.

performance details provided in Table 1. The compositions of thin films are classic (p-type $\text{Bi}_{0.5}\text{Sb}_{1.5}\text{Te}_3$ and n-type $\text{Bi}_2\text{Te}_{2.7}\text{Se}_{0.3}$), which have been previously demonstrated to possess high ZT values due to the optimization of n_p and n_e ^{10,11}. Notably, the S values in this work are significantly higher than that of the majority of BTS and BST thin films reported in the literature and prepared by magnetron sputtering^{11,40}. In addition to the well-designed classical compositions that demonstrate finely tuned n_p and n_e to achieve high S while maintaining sufficient σ for high $S^2\sigma$ values^{41–43}, the enhanced S is also largely attributed to the effective mass (m'), where a larger m' generally results in a higher S . The larger m' is related to the micro-nanostructure of our films, which have relatively good crystallinity and well-ordered crystal-crystal interfaces⁴¹.

We also conducted detailed characterizations of the thin films used in the devices. Figure 2a, b show the X-ray diffraction (XRD) patterns of the n-type BTS and p-type BST thin films deposited on PI substrates. Both films exhibit strong (015) orientation without any

impurity peaks, indicating their high anisotropies. BTS and BST possess similar crystal structures^{10,11}. In our previous work, we have demonstrated that (015)-oriented bismuth-telluride-based films exhibited optimized carrier mobility (μ)^{25,41–43}, contributing to their superior thermoelectric performance. Therefore, through accumulated experience, we optimized the magnetron sputtering process and strictly controlled the film growth orientation to achieve μ optimization. The photos of these films in flat states and their scanning electron microscopy (SEM) images from both top and cross-sectional views are included as insets in Fig. 2a, b. Both films exhibit high flexibility, attributed to their relatively uniform orientation and good crystallinity. The SEM images reveal dense films with excellent crystallinity and uniform crystal orientation, confirming the above arguments.

Figure 2c, d present spherical aberration-corrected scanning transmission electron microscopy (Cs-STEM) high-angle annular detector dark-field (HAADF) and bright-field (BF) images of the BTS film, while Fig. 2e, f show Cs-STEM HAADF and BF images of the BST

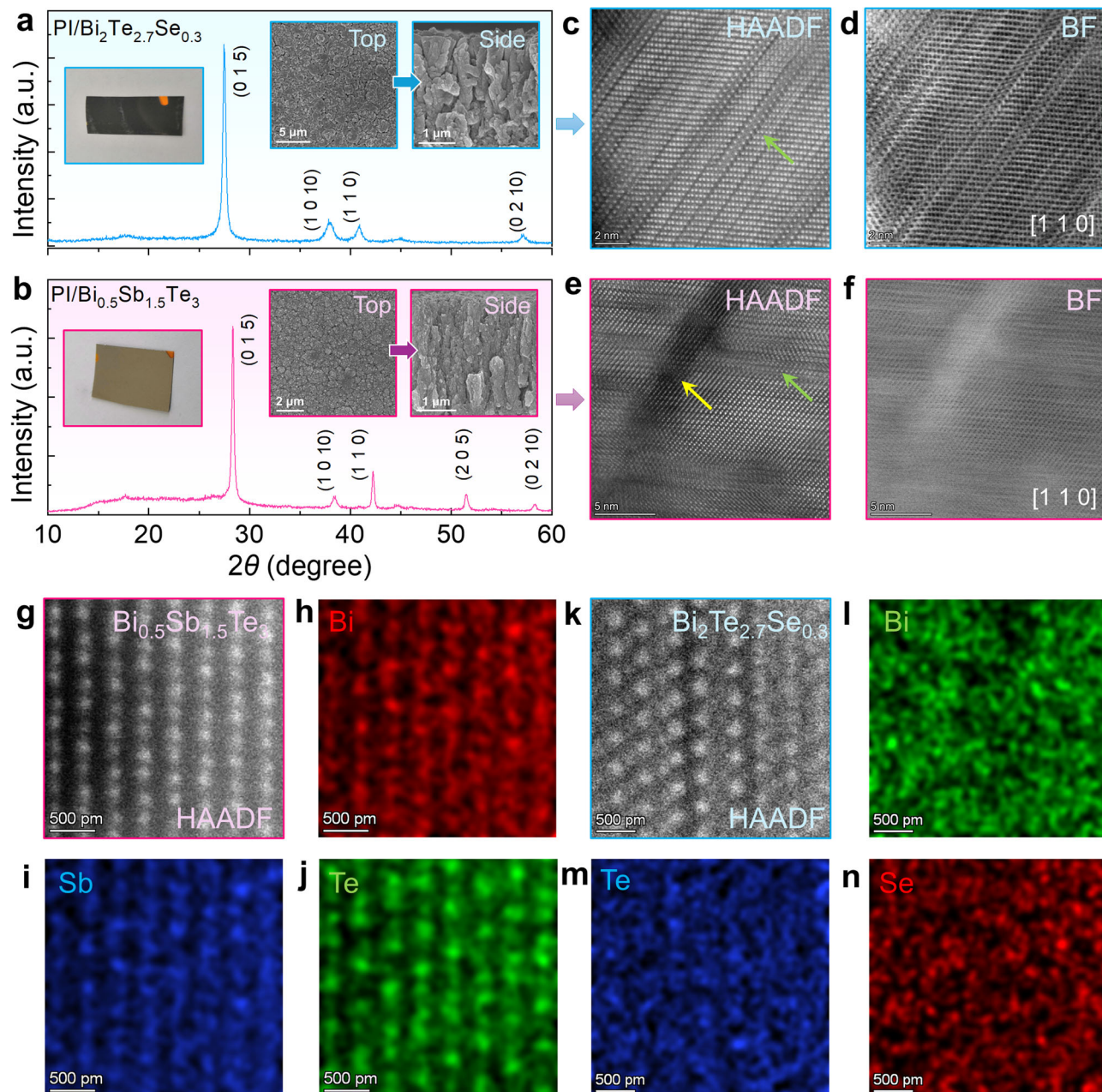


Fig. 2 | Characterizations of p-type and n-type thermoelectric thin films used in the flexible device. **a, b** X-ray diffraction (XRD) patterns of n-type $\text{Bi}_2\text{Te}_{2.7}\text{Se}_{0.3}$ (BTS) and p-type $\text{Bi}_{0.5}\text{Sb}_{1.5}\text{Te}_3$ (BST) thin films on PI substrates. The photos of these films in flat states and their scanning electron microscopy (SEM) images from both top and cross-sectional views are included as insets. Spherical aberration-corrected scanning transmission electron microscopy (Cs-STEM) **(c)** high-angle annular detector dark-field (HAADF) and **(d)** bright-field (BF) images of BTS film. The green

arrow indicates the potential line-type point defects. Cs-STEM **e** HAADF and **f** BF images of BST film. The yellow arrow indicates the potential grain boundary. **g** High-resolution Cs-STEM-HAADF image of BST film and corresponding energy dispersive X-ray spectroscopy (EDS) maps for element **h** Bi, **i** Sb, and **j** Te. **k** High-resolution Cs-STEM-HAADF image of BTS film and corresponding EDS maps for element **l** Bi, **m** Te, and **n** Se.

film (high-resolution images are provided in Supplementary Figs. 4, 5 for reference). By carefully tuning the zone axis, the view directions of both films are adjusted to the $[110]$ direction for convenient observation and comparison (the crystallographic direction indexing process can be referenced in Supplementary Figs. 6, 9). The 3% error in the index results is speculated to arise from slight deviations in local composition leading to slight lattice constant discrepancies, as well as slight zone axis deviations, which are considered normal phenomena and understandable. It can be observed that, although the films exhibit good macroscopic crystallinity, they still possess significant lattice defects at the nanoscale. These defects include linear point defects

(generally resulting from local lattice distortion due to composition segregation at the nanoscale) and atomic points with varying brightness (usually arising from differences in ion radii, such as Bi/Sb sites in BST and Te/Se sites in BTS, as shown in Supplementary Figs. 6–9). These nano-defects combined with grain boundaries can effectively scatter phonons with different wavelengths, leading to relatively low κ_l and contributing to the enhancement of ZT . Figure 2g presents the high-resolution Cs-STEM-HAADF image of the BST film, while Fig. 2h–j display the corresponding energy dispersive X-ray spectroscopy (EDS) maps for elements Bi, Sb, and Te. Similarly, Fig. 2k shows the high-resolution Cs-STEM-HAADF image of the BTS film, and Fig. 2l–n exhibit

the corresponding EDS maps for elements Bi, Te, and Se. High-quality corresponding BF images are available in Supplementary Figs. 10–11. It can be observed that atomic points with varying brightness confirm the earlier argument. Therefore, in summary, the high μ value of the film stems from its high anisotropy, leading to high σ , while the high S of the film comes from classical compositional design. Thus, the $S^2\sigma$ of the film can reach around $40 \mu\text{W cm}^{-1} \text{K}^{-2}$ at room temperatures. Besides, the internal interfaces such as grain boundaries and intensive nanoscale lattice imperfections such as point defects effectively scatter phonons, resulting in low κ and κ_t . The ultra-high ZT values of around 1.4 for both films are highly comparable to those reported for both bulk and flexible film-based bismuth telluride systems^{10,11}. Additionally, because the thin films are grown on flexible PI substrates, there are slight differences in orientations and compositions during the crystallization processes compared to growth on rigid substrates, as observed in our previous work^{25,41–43}, leading to slight differences in the as-achieved ZT values, which is understandable. Besides, it is also worth noting that our tests for electrical and thermal transport performance were both conducted along the in-plane direction of the thin film (see experimental details), thus resulting in the obtained ZT reflecting the in-plane performance, while the transport of heat and electricity within the device occurs in the out-of-plane direction of the film. However, considering the anisotropy of bismuth-telluride-based materials^{10,11}, we referenced the thermal and electrical transport properties of single-crystal Bi_2Te_3 in different directions^{44–46} to determine that the difference in ZT between the in-plane and out-of-plane directions of our thin film is relatively small (fluctuating by approximately 20% or less). This discrepancy has minimal impact on accurately assessing the device output performance.

Characterizations of functional layers

In our previous work²⁵, we reported the use of a nanometer-thick Ti layer as a barrier layer to enhance the adhesion between Cu electrodes and BTS or BST thin-film-based thermoelectric legs and effectively reduce the R_{in} of the device. This approach proved highly effective for rigid thin-film-based thermoelectric devices²⁵. Other works also report that Ti layers serve effectively as “diffusion barriers” to prevent diffusion and reduce contact resistance in bulk devices or rigid film materials. For example, one study discussed using a Ti barrier layer with low Young’s modulus and particle slip synergy to mitigate interface stress in bismuth telluride thermoelectric generators, resulting in an ideal interface with high thermal stability, high strength, and low electrical resistivity⁴⁷. Another study reported that introducing a Ti layer and controlling its thickness can regulate interface stability at the $\text{Bi}_2\text{Te}_3/\text{Cu}$ junction, prevent element diffusion, reduce contact resistance, and maintain mechanical strength⁴⁸. Additionally, researchers addressed controllable electrical contact resistance between Cu and oriented Bi_2Te_3 films by tuning the interface with the Ti layer⁴⁹. However, the reported role of the Ti layer is only a “diffusion barrier”, and there remains a significant research gap in the bonding between the electrode and the flexible organic substrate in flexible thermoelectric devices, which is crucial for further enhancing the device’s overall flexibility and stability. For flexible devices, the bonding strength between the inorganic Cu electrode and the organic PI flexible substrate is much weaker compared to that with rigid inorganic substrates like aluminum oxide. This weaker bonding strength inevitably leads to interface fracture between the Cu electrode and flexible substrate during repeated bending, resulting in device failure⁷. Therefore, to address this issue, in addition to co-sputtering a nanometer-thick Ti barrier layer between the Cu electrode layer and thin-film-based thermoelectric legs in our designed flexible devices, we also sputtered a nanometer-thick Ti contact layer between the Cu electrode and the PI flexible substrate. The choice of Ti material for this contact layer was for the convenience of the co-deposition process, and the thickness of the Ti contact layer was controlled to be within 10 nm. This thickness

allows the Ti contact layer to enable more effective bonding between the organic PI substrate and the inorganic Cu electrode portion. This constitutes the core highlight of our work.

To characterize the as-designed functional Ti layers, the structure of the thin-film-based thermoelectric device is illustrated in Fig. 3a. From the substrate to the thermoelectric legs, the components are PI (flexible substrate), Ti contact layer (Ti-2), Cu (electrode), Ti barrier layer (Ti-1), and thermoelectric thin films (BTS or BST). Figure 3b presents the XRD results of PI/Ti-2/Cu/Ti-1/BTS (top) and PI/Ti-2/Cu/Ti-1/BST (bottom). XRD peaks of the Cu electrode and thermoelectric thin films can be successfully indexed; however, due to the small thickness (around 10 nm as predicted by deposition parameters), the testing precision of XRD is insufficient to accurately characterize the nanoscale Ti contact layer and the contact layer. The cross-sectional SEM images of the PI/Ti-2/Cu/Ti-1/BST and PI/Ti-2/Cu/Ti-1/BTS samples, shown in Fig. 3c, d, depict sections of the devices prior to flip bonding. It can be observed that besides the thermoelectric thin films, the Cu electrode also exhibits good crystallinity, and there is good adhesion between the thermoelectric thin films and the Cu electrode, as well as between the Cu electrode and the PI flexible substrate. Figure 3e, f show the corresponding EDS line scan results, with the scan direction along from the thermoelectric thin films to the PI flexible substrate. Due to the small thickness of the Ti contact layer and contact layer, their existence is still difficult to characterize under SEM-based EDS. Figure 3g, h show cross-sectional SEM images of the PI/Cu/BST and PI/Cu/BTS samples, illustrating sections of the devices prior to flip bonding, specifically without Ti layers. It is evident that in the absence of Ti layers, there are clear interfaces between the thermoelectric thin films and the Cu electrode, as well as the Cu electrode and the PI film, indicating poor adhesions (especially between the Cu electrode and the PI film due to their distinct physical behaviors), thus demonstrating the crucial role of Ti layers in ensuring the adhesion between different components in the device.

To accurately characterize the presence of the Ti contact layer and barrier layer (especially the contact layer) and study their nanoscale interface behavior, we conducted Cs-STEM high-resolution characterization. Figure 4a shows a Cs-STEM-HAADF image of the cross-sectional view of PI/Ti-2/Cu/Ti-1/BST. From this image, it can be observed that the BST thin film exhibits varying contrasts, originating from grain boundaries or dense linear point defect regions. Additionally, the interfaces between different components are tightly connected. Figure 4b presents the corresponding EDS map for the overlap of C, Ti, Cu, Pt, and Bi elements, while individual element EDS maps can be found in Supplementary Fig. 12. Roughly, the upper and lower Ti layers can be discerned, with the upper layer being the Ti barrier layer between the BST thin film and Cu electrode, as indicated by its clear high-resolution image and corresponding EDS maps in Supplementary Fig. 13. The lower layer serves as the Ti contact layer between the Cu electrode and PI flexible substrate, as shown in Fig. 4c with its high-resolution EDS map for the overlap of C, Ti, and Cu elements, while other individual element EDS maps can be referenced in Supplementary Fig. 14. Essentially, C, N, and O elements originate from the PI substrate, while Pt is from the surface of the thin film (characterization requiring the deposition of a Pt layer). It is evident that compared to the upper Ti barrier layer, the actual thickness of the lower Ti contact layer is smaller, attributed to the loss of Ti when deposited on the organic PI substrate via magnetron sputtering, even though the preset deposition parameters for both Ti layers are the same (i.e., theoretical thicknesses are equal). The thickness of both Ti layers remains relatively uniform and does not change with the position of the thin film, as evidenced by the characterization results at another position of the BST thin film (Supplementary Fig. 15). Correspondingly, Fig. 4d shows a Cs-STEM-HAADF image of the cross-sectional view of PI/Ti-2/Cu/Ti-1/BTS, and Fig. 4e presents the corresponding EDS map for the overlap of C, Ti, Cu, Te, and Pt elements,

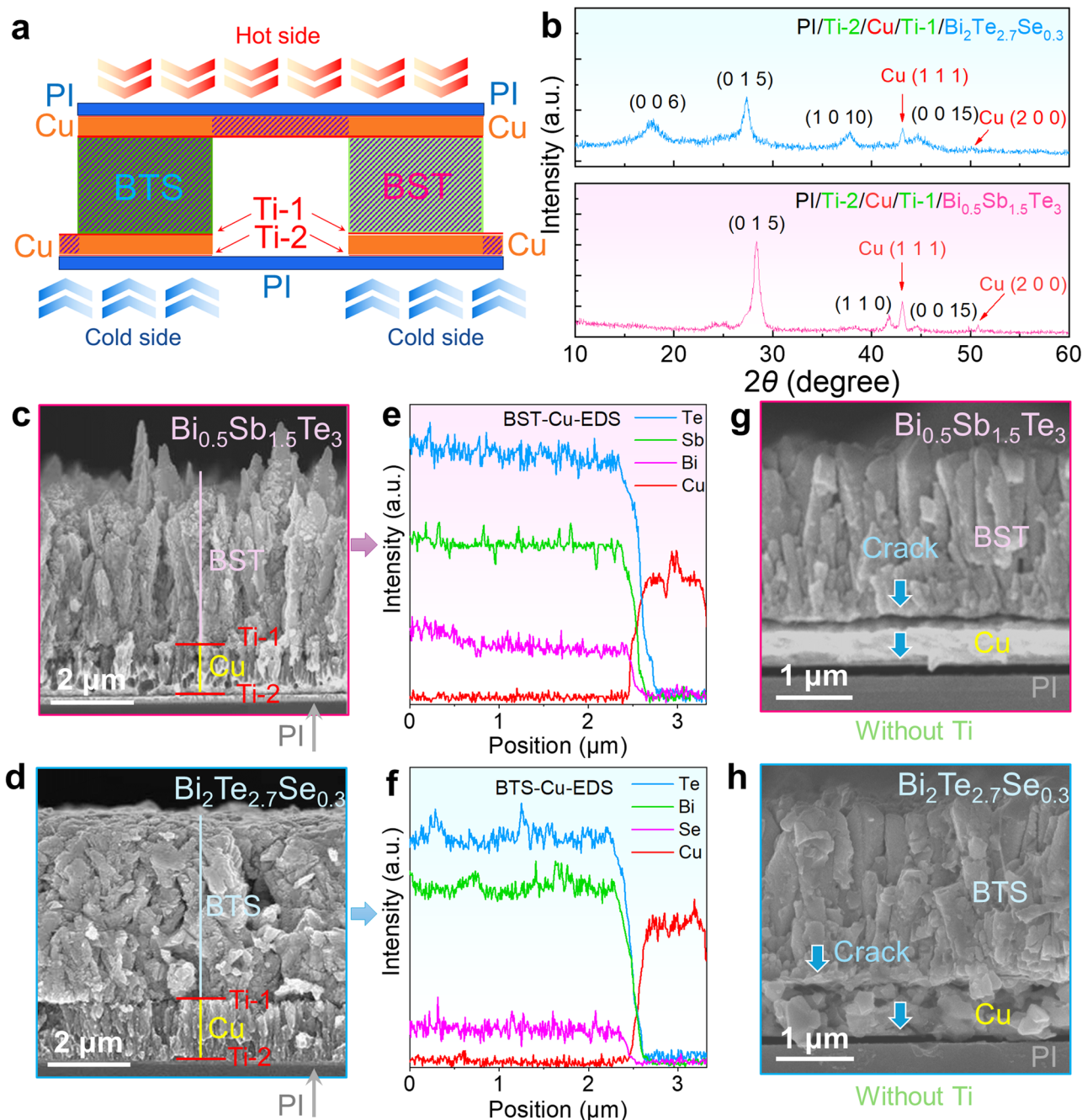


Fig. 3 | Characterizations of thin-film-based thermoelectric devices.

a Illustration of the structure of the thin-film-based thermoelectric device. From the substrate to the thermoelectric legs, the components are PI (flexible substrate), Ti contact layer (Ti-2), Cu (electrode), Ti barrier layer (Ti-1), and thermoelectric thin

films (BTS or BST). b XRD results of PI/Ti-2/Cu/Ti-1/BTS (top) and PI/Ti-2/Cu/Ti-1/BST (bottom). c, d SEM images of PI/Ti-2/Cu/Ti-1/BST and PI/Ti-2/Cu/Ti-1/BTS from cross-sectional views. e, f Corresponding EDS line scan results. g, h SEM images of PI/Cu/BST and PI/Cu/BTS from cross-sectional views (without Ti layers).

with individual element EDS maps provided in Supplementary Fig. 16. Characterization of the Ti barrier layer can be found in Supplementary Fig. 17. Figure 4f displays a magnified EDS map of PI/Ti-2/Cu for the overlap of N, Ti, and Cu elements, with other individual element EDS maps available in Supplementary Fig. 18. Essentially, the interface characterization results of PI/Ti-2/Cu/Ti-1/BTS are similar to those of PI/Ti-2/Cu/Ti-1/BST. Furthermore, besides the thin-film thermoelectric materials, the crystallinity of the Cu electrode is also excellent, as evident from its high-resolution Cs-STEM-HAADF images (Supplementary Fig. 19). Figure 4g displays the high-resolution Cs-STEM-BF image of PI/Ti-2/Cu for PI/Ti-2/Cu/Ti-1/BST, while Fig. 4h, i show high-resolution Cs-STEM BF and HAADF images of PI/Ti-2/Cu for PI/Ti-2/Cu/Ti-1/BTS.

Ti-1/BTS. Their higher-resolution images can also be referenced in Supplementary Figs. 20–21 for better comparison. It can be observed that between the inorganic Cu with a typical lattice structure and the organic PI substrate, which lacks any lattice information features, there is a gradient in the lattice at the Ti contact layer. This gradient feature indicates a progressive bonding between Cu and PI, without a distinct interface, leading to a very tight bonding between the Cu electrode and PI substrate.

To further demonstrate that Ti as a contact layer can enhance the bonding strength between the PI substrate and the Cu electrode, a Cu film (~800 nm) was deposited on the PI substrate. Ti and Cu films (Ti/Cu ~10 nm/800 nm) were sequentially deposited on the PI

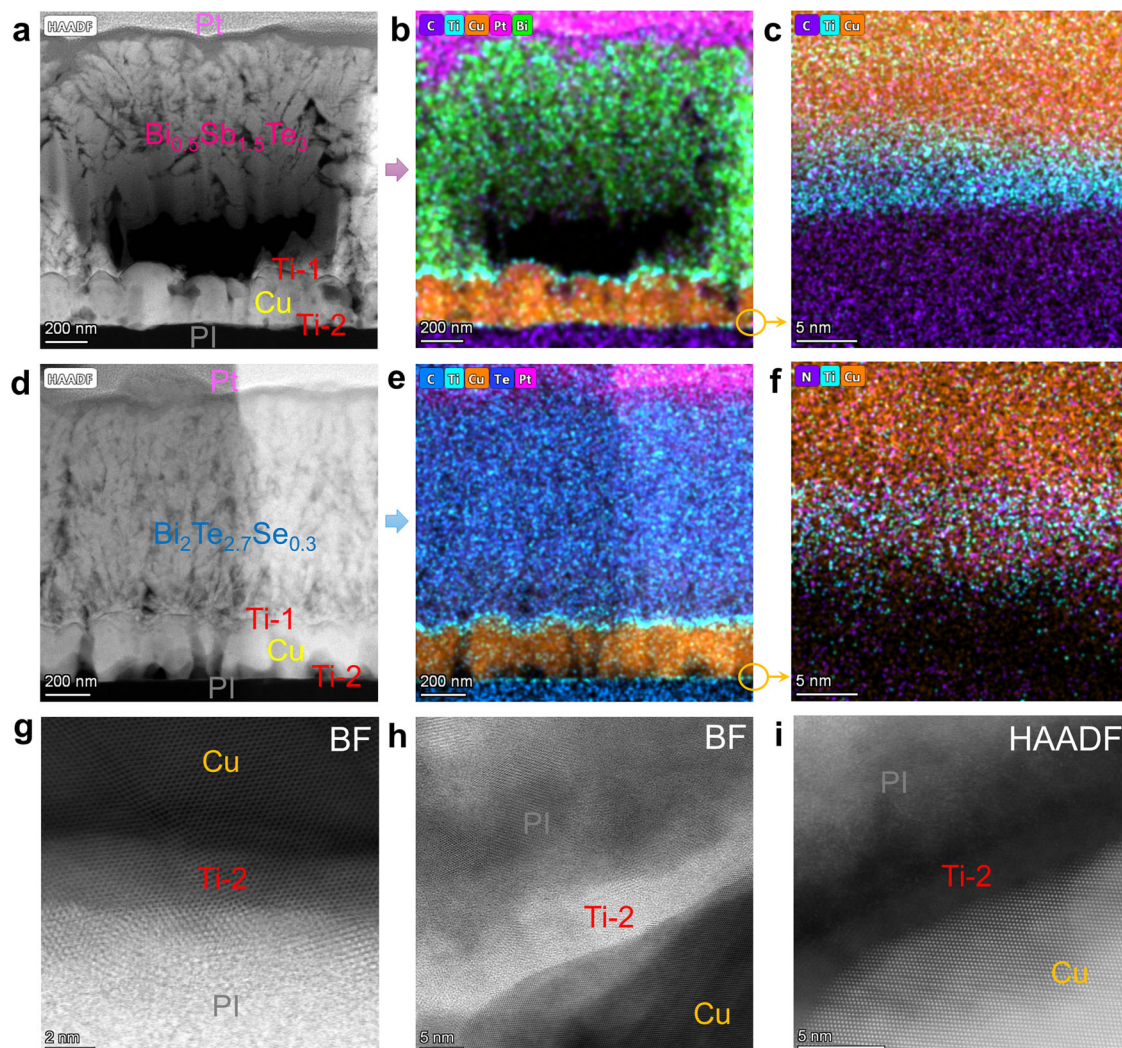


Fig. 4 | Characterizations of Ti contact layer between Cu electrode and PI substrate. **a** Cs-STEM-HAADF image of a cross-sectional view of PI/Ti-2/Cu/Ti-1/BST and **b** corresponding EDS map for overlap of C, Ti, Cu, Pt, and Bi elements. **c** Magnified EDS map of PI/Ti-2/Cu for overlap of C, Ti, and Cu elements. **d** Cs-STEM-HAADF image of a cross-sectional view of PI/Ti-2/Cu/Ti-1/BTS and corresponding

e EDS map for overlap of C, Ti, Cu, Te, and Pt elements. **f** Magnified EDS map of PI/Ti-2/Cu for overlap of N, Ti, and Cu elements. **g** High-resolution Cs-STEM-BF image of PI/Ti-2/Cu for PI/Ti-2/Cu/Ti-1/BST. **h,i** High-resolution Cs-STEM BF and HAADF images of PI/Ti-2/Cu for PI/Ti-2/Cu/Ti-1/BTS.

substrate under conditions of 473 K and 2 Pa using a magnetron sputtering system. Nano scratch tests were conducted using the Nano Indenter XP system. As shown in Supplementary Fig. 22, the scratch curve related to film failure rapidly drops to around 45 mN and exhibits a sharp discontinuity, indicating that the Cu film will peel off or rupture when the indenter impacts the Cu film. In contrast, the scratch depth of the Cu/Ti film shows no significant discontinuity (see Supplementary Fig. 22). This suggests that Ti/Cu films exhibit excellent adhesion to the flexible PI substrate, demonstrating significant potential for interconnections/electrodes in flexible electronic devices.

Flexibility and output performance of thin-film-based devices

To understand the crucial role of the Ti contact layer on device flexibility, we designed flexible devices with and without Ti contact layers (Ti-2) and evaluated their device flexibility. Figure 5a illustrates the measured overall resistance R of the devices with and without Ti contact layers (Ti-2) as a function of r (both with Ti barrier layers, Ti-1). The inset shows a photo illustrating the bending test, which can also be referenced in Supplementary Fig. 23. It can be observed that compared to the flexible device without the Ti contact layer, the flexible device with the Ti contact layer exhibits lower R under bending at any r values.

Figure 5b presents the R of the devices with and without Ti contact layers (Ti-2) as a function of the bending cycle (both with Ti barrier layers, Ti-1), with a r of 10 mm. The inset shows a photo illustrating the device in a considerably bent status. The flexible device without the Ti contact layer experiences a significant increase in R after more than 60 bends, and when the bending cycles exceed 100, R becomes infinite, indicating a result of device damage due to internal interface fracture caused by multiple bends. In contrast, the flexible device with the Ti contact layer shows a $\Delta R/R_0$ of only about 3% after bending more than 100 times, demonstrating the significant improvement in device flexibility attributed to the Ti contact layer.

In addition to the device flexibility, we also designed flexible devices with and without double Ti layers (Ti-1 and Ti-2) and evaluated their output performance. Figure 5c, d depict the open-circuit voltage V and P of the devices as a function of loading current / under different ΔT s. Measured V and P as a function of ΔT with and without double Ti layers can also be referenced in Supplementary Fig. 24. The highest device performance for these two cases is also shown in Table 2 for comparison. It can be observed that the flexible device with double Ti layers exhibits much higher V and P at the same ΔT , resulting in its extremely high ω , as shown in Fig. 5e. Figure 5f

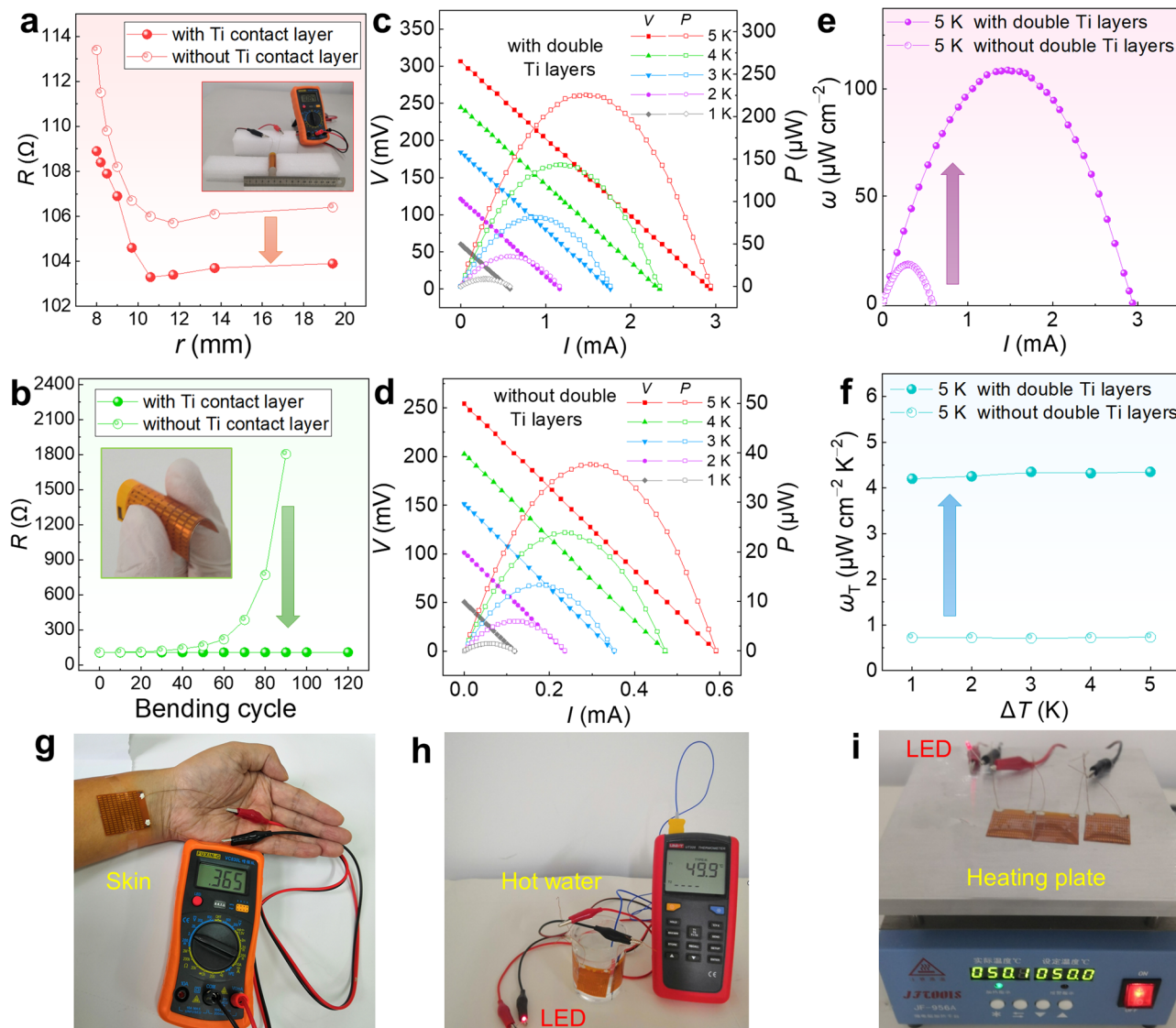


Fig. 5 | Thermoelectric performance and flexibility of thin-film-based devices. **a** Resistance R of the devices with and without Ti contact layers (Ti-2) as a function of bending radius r . The inset shows a photo that illustrates the bending test. **b** R of the devices with and without Ti contact layers (Ti-2) as a function of the bending cycle. The inset shows a photo that illustrates the device in a considerably bent status. Please note that both devices possess the Ti barrier layers (Ti-1). **c, d** Open-circuit voltage V and output power P of the devices with and without double Ti layers (Ti-1 and Ti-2) as a function of loading current I under different ΔT s.

e Measured output power density ω of the devices as a function of I under a ΔT of 5 K. **f** Determined ω_T of the devices as a function of ΔT . **g** Photo illustrating the flexible device composed of 162 pairs of n/p flexible thin films that can generate a voltage of 365 mV using the ΔT between the human body and the environment. **h** Photo illustrating the three flexible devices that can power an LED using the ΔT between the beaker with 50 °C hot water and the environment. **i** Photo illustrating the three flexible devices that can power an LED using the ΔT between the heating plate kept at 50 °C and the environment.

Table 2 | Thermoelectric performance of thin-film-based flexible devices with and without double Ti layers

Type	p-n pair	R_{in} (Ω)	R_c (Ω)	ΔT (K)	V (mV)	P (μ W)	ω (μ W cm^{-2})	ω_T (μ W $\text{cm}^{-2} \text{K}^{-2}$)
With double Ti layers	162	104.2	63.7	5	306.5	225.4	108.7	4.35
Without double Ti layers	162	428.8	388.3	5	254.2	37.7	18.2	0.73

Here R_{in} , R_c , ΔT , V , P , ω , and ω_T denote device internal resistance, contact resistance, temperature difference, open-circuit voltage, output power, output power density, and normalized power density, respectively.

illustrates the determined ω_T of the devices as a function of ΔT . It can be seen that the flexible device with double Ti layers achieves a ω_T of 4.35 μ W $\text{cm}^{-2} \text{K}^{-2}$, far exceeding that of the flexible device without double Ti layers and previously reported results (refer to Supplementary Table 1).

In this work, we optimized the Ti contact layer thickness to approximately 10 nm. As shown in Supplementary Table 2, devices with a Ti contact layer thickness of about 10 nm exhibited the best

output performance. If the Ti contact layer is too thick, it may obstruct heat transfer and reduce the device's output performance ($\kappa_{Ti} = -15 \text{ W m}^{-1} \text{K}^{-1}$ and $\kappa_{Cu} = -380 \text{ W m}^{-1} \text{K}^{-1}$). Conversely, when the Ti contact layer is only a few nanometers thick or absent, it is challenging to achieve a tight bond between the electrode and the PI substrate (see Figs. 3g, h), leading to a decline in the device's performance. Additionally, we conducted extra bending failure experiments to demonstrate that flexible devices with a multilayer film structure are prone to

initial fracture at the Ti barrier layer by flip-chip bonding during repeated bending. We sequentially deposited Ti, Cu, and Ti films onto PI substrates using a magnetron sputtering system under conditions of 473 K and 2 Pa, forming PI/Ti/Cu/Ti samples (Supplementary Figs. 25a, b). Similarly, PI/Ti/Cu/Ti/BTS and PI/Ti/Cu/Ti/BST samples were prepared under the same conditions (Supplementary Figs. 25a, c, d). Subsequently, PI/Ti/Cu/Ti/BTS/Ti/Cu/Ti/PI and PI/Ti/Cu/Ti/BST/Ti/Cu/Ti/PI samples were fabricated through bonding and annealing at 423 K. Both multilayer films underwent approximately 500 cycles of bending until they loosened and peeled off. As shown in Supplementary Figs. 25e–25h, the fractured contact surfaces at the Ti barrier layer due to flip-chip bonding are clearly visible in the PI/Ti/Cu/Ti/BTS/Ti/Cu/Ti/PI and PI/Ti/Cu/Ti/BST/Ti/Cu/Ti/PI multilayer samples. However, the images reveal that the electrode and thermoelectric materials remained interconnected and interwoven through the hot-press bonding method, ensuring excellent film flexibility. Subsequently, residual PI/Ti/Cu/Ti/BTS and PI/Ti/Cu/Ti/BST films, derived from the PI/Ti/Cu/Ti/BTS/Ti/Cu/Ti/PI and PI/Ti/Cu/Ti/BST/Ti/Cu/Ti/PI samples, were subjected to additional bending cycles (~800 cycles) until they became loose and peeled off. The fractured surfaces of the PI/Ti/Cu/Ti/BTS and PI/Ti/Cu/Ti/BST multilayer films, shown in Supplementary Figs. 25i–l, exhibit noticeably irregular features at the Ti barrier layer, which was directly deposited. This indicates that the thermoelectric materials adhered well to the electrodes and maintained strong growth. In summary, the PI/Ti/Cu/Ti/BTS/Ti/Cu/Ti/PI and PI/Ti/Cu/Ti/BST/Ti/Cu/Ti/PI multilayer samples are prone to initial fractures at the Ti barrier layer during flip-chip bonding. After repeated bending, fractures also initiated at the directly deposited Ti barrier layer. Nevertheless, neither multilayer film loosened or peeled off at the Ti contact layer during the experiment. The introduction of the Ti contact layer remains crucial for enhancing bonding and mechanical stability, even though fractures were observed at the Ti barrier layer under cyclic bending. Additional EDS results are provided in Supplementary Figs. 26–27 for reference. Besides, we verified why we used 423 K as the annealing temperature. This is because a temperature that is too low (e.g., 373 K) leads to poor adhesion between the Ti barrier layer and the BST or BTS films (Supplementary Figs. 28a–d), while a temperature that is too high (e.g., 573 K) causes deformation of the PI substrate, resulting in partial delamination of the electrode material from the PI substrate at the Ti contact layer (Supplementary Figs. 28e–f). The effects of annealing temperature and the Ti layers, especially the Ti barrier layers, on the flexibility of flexible devices and their overall thermoelectric performance can be referenced in Supplementary Figs. 29–30 and Supplementary Tables 3–5. Additional experimental evidence supporting that the Ti contact layer effectively enhances device flexibility can be found in Supplementary Fig. 31. Moreover, experimental evidence indicating that no significant Ti doping or diffusion occurred^{50,51} during the experimental design process can be found in Supplementary Fig. 32. The bond strength measurement indicates that the device begins to peel off at the Ti barrier layer during flip-chip bonding when the tensile force reaches 25.1 N (see Supplementary Fig. 33 and Supplementary Movie 1).

Due to the high flexibility and outstanding ω_T with just a few Kelvins of ΔT , the application scenarios of our designed devices have been greatly expanded. The most remarkable feature is that they do not even require any additional heat dissipation parts (such as heat sinks) or amplifiers (boosters). Simply placing them on an irregular heat source with a certain temperature, when reaching equilibrium, the device can maintain a stable ΔT of a few Kelvins across its two sides. Such a small ΔT is sufficient to drive many low-grade electronics, marking a revolutionary breakthrough in flexible thermoelectrics. As shown in Fig. 5g, a photo illustrates the flexible device composed of 162 pairs of n/p flexible thin films that can generate a voltage of 365 mV

using the ΔT between the human body and the environment. This output voltage is sufficient to power many wearable electronic devices such as sensors⁷. Figure 5h displays a photo illustrating three flexible devices that can power an LED using the ΔT between a round and smooth beaker with 50 °C hot water and the environment, with an output voltage of up to 1.85 V. Additionally, Fig. 5i illustrates a photo illustrating three flexible devices that can power an LED using the ΔT between the heating plate kept at 50 °C and the environment (refer to Supplementary Movie 2), with an output voltage of up to 1.84 V. It is evident that as long as the temperature of the heat source is maintained, the flexible devices can generate electricity for a long time, greatly expanding their application scenarios. For example, we can directly use light irradiation on their surface for power generation (refer to Supplementary Movie 3), serving as fast and efficient photo-thermal flexible conversion devices, demonstrating their enormous potential in cross-energy application fields and functional device integration.

In conclusion, for the first time, we achieved highly flexible thermoelectric devices with outstanding thermoelectric performance. This device consists of 162 pairs of flexible thin films with high room-temperature ZT values for both p-type BST ($ZT=1.39$) and n-type BTS ($ZT=1.44$), prepared using a combination of magnetron sputtering and flip-chip bonding techniques. The device demonstrates a ω of $108 \mu\text{W cm}^{-2}$ under a small ΔT of 5 K, and a ω_T exceeding $4 \mu\text{W cm}^{-2} \text{ K}^{-2}$, which are highly competitive compared to reported results. The ultra-high device performance stems from the unique interface design of the PI substrate/Ti contact layer/Cu electrode/Ti barrier layer/thermoelectric thin film. The nano-sized Ti contact layer tightly bonded the organic PI substrate and Cu electrode, resulting in exceptional device flexibility. Additionally, the Ti barrier layer significantly reduces the R_{in} of the device and enhances the tightness between the Cu electrode and the thermoelectric thin film, enabling the device to achieve both ultra-high P and flexibility. The device is susceptible to initial fractures at the Ti barrier layer during flip-chip bonding under repeated cyclical bending. Three series-connected devices attached to an irregular heat source at 50 °C (such as a heater pipe) can output a voltage of 1.85 V and illuminate an LED without the need for any heat sink or booster, demonstrating outstanding performance and high flexibility. This work greatly enhances the application capabilities of flexible thermoelectric devices and demonstrates their commercialization potential.

Methods

Film fabrication

In this study, p-type $\text{Bi}_{0.5}\text{Sb}_{1.5}\text{Te}_3$ and n-type $\text{Bi}_{2}\text{Te}_{2.7}\text{Se}_{0.3}$ films were deposited at a temperature of 473 K and a working pressure of 2 Pa using a magnetron sputtering system. Commercial $\text{Bi}_{0.5}\text{Sb}_{1.5}\text{Te}_3$ and $\text{Bi}_{2}\text{Te}_{2.7}\text{Se}_{0.3}$ targets with a diameter of 50 mm (purchased from the General Research Institute for Nonferrous Metals, China) were utilized for sputtering. The direct-current powers applied to the targets were set to 25 W for both $\text{Bi}_{0.5}\text{Sb}_{1.5}\text{Te}_3$ and $\text{Bi}_{2}\text{Te}_{2.7}\text{Se}_{0.3}$. Ti and Cu targets, each with a purity of 99.99%, were sputtered at 35 W and 30 W, respectively, for the deposition of Ti and Cu films under the same conditions of temperature and pressure. The base pressure was maintained below 2×10^{-4} Pa. Before deposition, PI substrates were thoroughly cleaned using diluted nitric acid and acetone, followed by drying under nitrogen airflow. The thickness of the thermoelectric films was approximately 2.5 μm , while the electrode Cu thickness was around 800 nm, and the Ti contact layer or Ti barrier layer was approximately 10 nm, achieved by controlling the deposition rate and sputtering time.

Device fabrication

Stainless steel masks with specified patterns were utilized to create devices electrically connected in series, consisting of a mask for the

thermoelectric film (mask_p) and masks for the electrodes (mask_e). Initially, connection metal pads of Ti, Cu, and Ti (or Ti, Cu; or Cu, Ti; or Cu) were deposited sequentially onto the lower and upper PI plates, each with a thickness of 0.25 mm, employing magnetron sputtering and mask_e -assisted deposition technology, respectively. The upper and lower PI plates measured 30 mm \times 30 mm and 35 mm \times 35 mm, respectively. Subsequently, p-type $\text{Bi}_{0.5}\text{Sb}_{1.5}\text{Te}_3$ and n-type $\text{Bi}_{2}\text{Te}_{2.7}\text{Se}_{0.3}$ film pairs, each with an area of 0.8 mm \times 0.8 mm, were deposited onto the metal pads (with a surface size of 0.8 \times 2.4 mm²) beneath mask_p . Finally, employing flip-chip bonding techniques, the upper PI plate with 162 p-type elements and the lower PI plate with 162 n-type elements were bonded together to form a module consisting of 162 pairs of p/n couples. Specifically, the n-type $\text{Bi}_{2}\text{Te}_{2.7}\text{Se}_{0.3}$ and p-type $\text{Bi}_{0.5}\text{Sb}_{1.5}\text{Te}_3$ plates were secured into designated slots to maintain alignment, followed by placing a 650 g weight on the slots to ensure proper contact (Supplementary Fig. 34). The assembled components were then subjected to sintering in an annealing oven at 373 K, 423 K, 473 K, and 573 K for 30 min each in an Ar atmosphere, followed by natural cooling to room temperature within the Ar atmosphere. The heat pressing method increases the kinetic energy at the interface, promoting atomic diffusion between the Ti layer and the thermoelectric or Cu films, which enhances the bonding process. Due to their higher surface energy and larger proportion of surface atoms, nanomaterials like a 10 nm Ti layer exhibit lower effective melting points compared to their bulk counterparts. This property enables the Ti layer to form strong bonds with other materials at relatively low temperatures, such as the 423 K used in this study. Furthermore, the 10 nm thickness of the Ti layer ensures sufficient interaction to bond the Cu electrode to the thermoelectric films and PI substrates effectively. The unique microstructure formation, as shown in Fig. 4 and Supplementary Figs. 12–18, further reinforces the bond strength.

Characterization

The crystal structures of the n-type $\text{Bi}_{2}\text{Te}_{2.7}\text{Se}_{0.3}$ and p-type $\text{Bi}_{0.5}\text{Sb}_{1.5}\text{Te}_3$ films grown on PI substrates were analyzed using XRD with Cu K α radiation ($\lambda = 0.154056$ nm) on a Rigaku D/MAX 2200 instrument. The morphology of the films and couples was observed via field-emission SEM using a Sirion 200 microscope. Compositional analysis was conducted using EDS. Further structural characterization of the films was carried out using Cs-STEM (Titan Cubed Themis G2 300, USA), with TEM samples prepared using a focused ion beam (FIB) technique based on the ZEISS CrossBeam 540 system. Surface profilometry to measure film thickness was performed using an Ambios XP-2 instrument. The nanoscratch test was conducted using a Nano Indenter XP system, with a maximum load of up to 75 mN to assess fracture resistance. The bond strength of the device was measured by the HT-8336 tensile test machine.

Thermoelectric performance evaluation

The σ and S were measured simultaneously on thin films deposited on 5 \times 15 \times 1 mm³ substrates using a ZEM-3 instrument (Ulvac Riko, Inc.). κ data were collected at room temperature using a Laser PIT instrument (Ulvac Riko, Inc.). n_e for n-type $\text{Bi}_{2}\text{Te}_{2.7}\text{Se}_{0.3}$ and n_p for p-type $\text{Bi}_{0.5}\text{Sb}_{1.5}\text{Te}_3$ and μ were determined via a four-probe measurement based on the Hall effect (ECOPIA HMS-3000) at room temperature. The power generation of the devices was assessed by applying a ΔT between the hot and cold sides. V , R , and P were measured using a Keithley 2450 source meter. Each test was repeated 10 times.

Data availability

The data generated in this study is provided in the Source Data file. Source data are provided with this paper.

References

- Shi, X. L., Zou, J. & Chen, Z. G. Advanced thermoelectric design: from materials and structures to devices. *Chem. Rev.* **120**, 7399–7515 (2020).
- Yang, Q. et al. Flexible thermoelectrics based on ductile semiconductors. *Science* **377**, 854–858 (2022).
- Chen, W. et al. Nanobinders advance screen-printed flexible thermoelectrics. *Science* **386**, 1265–1271 (2024).
- Zhang, L., Shi, X. L., Yang, Y. L. & Chen, Z. G. Flexible thermoelectric materials and devices: from materials to applications. *Mater. Today* **46**, 62–108 (2021).
- Xu, S. et al. Conducting polymer-based flexible thermoelectric materials and devices: from mechanisms to applications. *Prog. Mater. Sci.* **121**, 100840 (2021).
- Blackburn, J. L., Ferguson, A. J., Cho, C. & Grunlan, J. C. Carbon-nanotube-based thermoelectric materials and devices. *Adv. Mater.* **30**, 1704386 (2018).
- Shi, X. L. et al. Advances in flexible inorganic thermoelectrics. *EcoEnergy* **1**, 296–343 (2023).
- Zhang, Q., Deng, K., Wilkens, L., Reith, H. & Nielsch, K. Micro-thermoelectric devices. *Nat. Electron.* **5**, 333–347 (2022).
- Eom, Y., Wijethunge, D., Park, H., Park, S. H. & Kim, W. Flexible thermoelectric power generation system based on rigid inorganic bulk materials. *Appl. Energ.* **206**, 649–656 (2017).
- Tang, X., Li, Z., Liu, W., Zhang, Q. & Uher, C. A comprehensive review on Bi_2Te_3 -based thin films: thermoelectrics and beyond. *Interdiscipl. Mater.* **1**, 88–115 (2022).
- Cao, T. et al. Advances in bismuth-telluride-based thermoelectric devices: progress and challenges. *eScience* **3**, 100122 (2023).
- Zhu, M., Shi, X. L., Wu, H., Liu, Q. & Chen, Z. G. Advances in Ag_2S -based thermoelectrics for wearable electronics: progress and perspective. *Chem. Eng. J.* **475**, 146194 (2023).
- Wu, H., Shi, X. L., Duan, J., Liu, Q. & Chen, Z. G. Advances in Ag_2Se -based thermoelectrics from materials to applications. *Energy Environ. Sci.* **16**, 1870–1906 (2023).
- Du, J. et al. Inkjet printing flexible thermoelectric devices using metal chalcogenide nanowires. *Adv. Funct. Mater.* **33**, 2213564 (2023).
- Xue, Y. et al. Constructing quasi-layered and self-hole doped SnSe oriented films to achieve excellent thermoelectric power factor and output power density. *Sci. Bull.* **68**, 2769–2778 (2023).
- Yang, D. et al. High thermoelectric performance of aluminum-doped cuprous selenide thin films with exceptional flexibility for wearable applications. *Nano Energy* **117**, 108930 (2023).
- Tian, R. et al. A solution-processed TiS_2 /organic hybrid superlattice film towards flexible thermoelectric devices. *J. Mater. Chem. A* **5**, 564–570 (2017).
- Zhou, Z. et al. Augmented near-room-temperature power factor of homogeneously grown thermoelectric ZnO films. *Appl. Phys. Lett.* **124**, 013903 (2024).
- Zheng, Z. H. et al. Harvesting waste heat with flexible Bi_2Te_3 thermoelectric thin film. *Nat. Sustain.* **6**, 180–191 (2023).
- Ao, D. W. et al. Assembly-free fabrication of high-performance flexible inorganic thin-film thermoelectric device prepared by a thermal diffusion. *Adv. Energy Mater.* **12**, 2202731 (2022).
- Yamamoto, H., Hatsuta, N., Wachi, M., Takei, Y. & Takashiri, M. Combination of electrodeposition and transfer processes for flexible thin-film thermoelectric generators. *Coatings* **8**, 22 (2018).
- Joo, S. J. et al. Fabrication of miniature thermoelectric generators using bulk materials. *J. Electron. Mater.* **45**, 3453–3459 (2016).

23. Zang, J. et al. Effect of post-annealing treatment on the thermoelectric properties of Ag_2Se flexible thin film prepared by magnetron sputtering method. *Res. Phys.* **45**, 106222 (2023).

24. Yang, S., Qiu, P., Chen, L. & Shi, X. Recent developments in flexible thermoelectric devices. *Small Sci.* **1**, 2100005 (2021).

25. Tan, M., Liu, W. D., Shi, X. L., Sun, Q. & Chen, Z. G. Minimization of the electrical contact resistance in thin-film thermoelectric device. *Appl. Phys. Rev.* **10**, 021404 (2023).

26. Liu, M., Li, W. & Pei, Y. Screening metal diffusion barriers for thermoelectric $\text{Bi}_{0.5}\text{Sb}_{1.5}\text{Te}_3$. *Sci. China Mater.* **67**, 289–294 (2024).

27. Ahmed, A. & Han, S. Fabrication, micro-structure characteristics and transport properties of co-evaporated thin films of Bi_2Te_3 on AlN coated stainless steel foils. *Sci. Rep.* **11**, 4041 (2021).

28. Xie, Z., Wang, J. & Yeow, J. T. W. Flexible multi-element photo-thermoelectric detectors based on spray-coated graphene/polyethylenimine composites for nondestructive testing. *ACS Appl. Mater. Interfaces* **15**, 5921–5930 (2023).

29. Mizoshiri, M., Mikami, M. & Ozaki, K. The effect of Cr buffer layer thickness on voltage generation of thin-film thermoelectric modules. *J. Micromech. Microeng.* **23**, 115016 (2013).

30. Ahmed, A. & Han, S. Optimizing the structural, electrical and thermoelectric properties of antimony telluride thin films deposited on aluminum nitride-coated stainless steel foil. *Sci. Rep.* **10**, 6978 (2020).

31. Sasaki, Y. & Takashiri, M. Effects of Cr interlayer thickness on adhesive, structural, and thermoelectric properties of antimony telluride thin films deposited by radio-frequency magnetron sputtering. *Thin Solid Films* **619**, 195–201 (2016).

32. Yang, D. et al. Flexible power generators by Ag_2Se thin films with record-high thermoelectric performance. *Nat. Commun.* **15**, 923 (2024).

33. Varghese, T. et al. Flexible thermoelectric devices of ultrahigh power factor by scalable printing and interface engineering. *Adv. Funct. Mater.* **30**, 1905796 (2020).

34. Choo, S. et al. Cu_2Se -based thermoelectric cellular architectures for efficient and durable power generation. *Nat. Commun.* **12**, 3550 (2021).

35. Banerjee, P. et al. Effect of particle-size distribution and pressure-induced densification on the microstructure and properties of printable thermoelectric composites and high energy density flexible devices. *Nano Energy* **89**, 106482 (2021).

36. Liu, Y. et al. Fully inkjet-printed Ag_2Se flexible thermoelectric devices for sustainable power generation. *Nat. Commun.* **15**, 2141 (2024).

37. Cao, J. et al. Flexible elemental thermoelectrics with ultra-high power density. *Mater. Today Energy* **25**, 100964 (2022).

38. Hou, S. et al. High performance wearable thermoelectric generators using Ag_2Se films with large carrier mobility. *Nano Energy* **87**, 106223 (2021).

39. Chang, P. S. & Liao, C. N. Screen-printed flexible thermoelectric generator with directional heat collection design. *J. Alloy. Compd.* **836**, 155471 (2020).

40. Hu, B. et al. Advances in flexible thermoelectric materials and devices fabricated by magnetron sputtering. *Small Sci.* **23**00061 <https://doi.org/10.1002/smss.202300061> (2023).

41. Tan, M. et al. In situ crystal-amorphous compositing inducing ultrahigh thermoelectric performance of p-type $\text{Bi}_{0.5}\text{Sb}_{1.5}\text{Te}_3$ hybrid thin films. *Nano Energy* **78**, 105379 (2020).

42. Tan, M. et al. Synergistic texturing and Bi/Sb-Te antisite doping secure high thermoelectric performance in $\text{Bi}_{0.5}\text{Sb}_{1.5}\text{Te}_3$ -Based thin films. *Adv. Energy Mater.* **11**, 2102578 (2021).

43. Tan, M. et al. Anisotropy control-induced unique anisotropic thermoelectric performance in the n-type $\text{Bi}_2\text{Te}_{2.7}\text{Se}_{0.3}$ thin films. *Small Methods* **3**, 1900582 (2019).

44. Fuschillo, N. & Gibson, R. Germanium-silicon, lead telluride, and bismuth telluride alloy solar thermoelectric generators for venus and mercury probes. *Adv. Energy Convers.* **7**, 43–52 (1967).

45. Frost, R. T., Corelli, J. C. & Balicki, M. Reactor irradiation PbTe , Bi_2Te_3 and ZnSb . *Adv. Energy Convers.* **2**, 77–78 (1962).

46. Bekebrede, W. R. & Guentert, O. J. Lattice parameters in the system antimony telluride bismuth telluride. *J. Phys. Chem. Solids* **23**, 1023–1025 (1962).

47. Sun, Y. et al. Performance boost for bismuth telluride thermoelectric generator via barrier layer based on low Young's modulus and particle sliding. *Nat. Commun.* **14**, 8085 (2023).

48. Qin, D., Zhu, W., Hai, F., Wang, C., Cui, J., & Deng, Y. Enhanced interface stability of multilayer $\text{Bi}_2\text{Te}_3/\text{Ti}/\text{Cu}$ films after heat treatment via the insertion of a Ti layer. *Adv. Mater. Interfaces* **6**, 1900682 (2019).

49. Kong, X. et al. Controllable electrical contact resistance between Cu and oriented- Bi_2Te_3 film via interface tuning. *ACS Appl. Mater. Interfaces* **9**, 25606–25614 (2017).

50. Gong, T. et al. Ultrahigh power factor of sputtered nanocrystalline n-type Bi_2Te_3 thin film via vacancy defect modulation and Ti additives. *Adv. Sci.* **11**, 2403845 (2024).

51. Hu, X. et al. Enhancement on thermoelectric performance by Ti doping and vacancies. *Mater. Today Phys.* **38**, 101255 (2023).

Acknowledgements

This work was financially supported by the National Natural Science Foundation of China (No. 61474082), the Tiangong University Start-up Grant, the Key Program of Natural Science Foundation of Tianjin, the Australian Research Council, the HBIS-UQ Innovation Centre for Sustainable Steel project, and the QUT Capacity Building Professor Program. This work was enabled using the Central Analytical Research Facility hosted by the Institute for Future Environments at QUT.

Author contributions

Z.-G.C. conceived the idea and supervised the overall experiments. M.T., X.-L.S., and Z.-G.C. designed the related experiments. M.T. prepared materials and measured the thermoelectric properties, designed device structures, fabricated devices, and measured the performance. X.-L.S., M.T., and Z.-G.C. analyzed the data. M.L. performed the device numerical simulation and calculations. W.-D.L., Y.J., S.L., T.C., W.C., T.L., Y.D., and S.L. discussed the results. X.-L.S. and Z.-G.C. wrote the manuscript with the help of all the authors.

Competing interests

The authors declare no competing interests.

Additional information

Supplementary information The online version contains supplementary material available at <https://doi.org/10.1038/s41467-025-56015-5>.

Correspondence and requests for materials should be addressed to Zhi-Gang Chen.

Peer review information *Nature Communications* thanks the anonymous reviewer(s) for their contribution to the peer review of this work. A peer review file is available.

Reprints and permissions information is available at <http://www.nature.com/reprints>

Publisher's note Springer Nature remains neutral with regard to jurisdictional claims in published maps and institutional affiliations.

Open Access This article is licensed under a Creative Commons Attribution-NonCommercial-NoDerivatives 4.0 International License, which permits any non-commercial use, sharing, distribution and reproduction in any medium or format, as long as you give appropriate credit to the original author(s) and the source, provide a link to the Creative Commons licence, and indicate if you modified the licensed material. You do not have permission under this licence to share adapted material derived from this article or parts of it. The images or other third party material in this article are included in the article's Creative Commons licence, unless indicated otherwise in a credit line to the material. If material is not included in the article's Creative Commons licence and your intended use is not permitted by statutory regulation or exceeds the permitted use, you will need to obtain permission directly from the copyright holder. To view a copy of this licence, visit <http://creativecommons.org/licenses/by-nc-nd/4.0/>.

© The Author(s) 2025